

# Experiment demonstration of tilt-to-length coupling suppression by beam-alignment-mechanism

**Peng Qiu, Xiang Lin, Hao Yan\*, Zebing Zhou**

Center for gravitational experiment, MOE Key Laboratory of Fundamental Physical Quantities Measurements, The School of Physics, Huazhong University of Science and Technology, Wuhan 430074, China

**Huizong Duan, Fan Zhu**

MOE Key Laboratory of TianQin Mission, TianQin Research Center for Gravitational Physics & School of Physics and Astronomy, Frontiers Science Center for TianQin, Gravitational Wave Research Center of CNSA, Sun Yat-sen University (Zhuhai Campus), Zhuhai 519082, China

**Haixing Miao**

State Key Laboratory of Low Dimensional Quantum Physics, Department of Physics, Tsinghua University, Beijing, China

E-mail: [yanhao2022@hust.edu.cn](mailto:yanhao2022@hust.edu.cn)

**Abstract.** Tilt-to-length (TTL) noise, caused by angular jitter and misalignment, is a major noise source in the inter-satellite interferometer for gravitational wave detection. However, the required level of axis alignment of the optical components is beyond the current state of the art. A set of optical parallel plates, called beam alignment mechanism (BAM), is proposed by LISA to compensate for the alignment error. In this paper, we show a prototype design of the BAM and demonstrate its performance in a ground-based optical system. We derive the BAM theoretical model, which agrees well with the numerical simulation. Experimental results reveal that the BAM can achieve lateral displacement compensation of the optical axis with a resolution of  $1\ \mu\text{m}$  across a dynamic range of about  $0.5\ \text{mm}$ . Furthermore, the TTL coefficient is reduced from about  $0.3\ \text{mm/rad}$  to about  $5\ \mu\text{m/rad}$ , satisfying the preliminary requirements for LISA and TianQin. These findings confirm the efficacy of the BAM in suppressing TTL noise, offering a promising solution for space-based gravitational wave detection.

*Keywords:* beam alignment mechanism, tilt-to-length coupling, interferometer, gravitational wave detection

## 1. Introduction

Gravitational wave detection has opened new windows into the universe, enabling the observation of phenomena such as black hole mergers and neutron star collisions [1].

Space-based gravitational wave detectors like LISA [2], TianQin [3, 4] and Taiji [5, 6] are poised to extend the observation window to low-frequency gravitational waves, enabling the detection of massive black hole mergers and the early universe’s stochastic gravitational wave background. However, despite the potential breakthroughs, space-based GW detectors face numerous technical challenges, with tilt-to-length (TTL) coupling noise emerging as one of the primary limitations for their sensitivity.

TTL coupling arises when angular misalignments in the optical system introduce unwanted length changes in the interferometric measurements. In current research, TTL coupling is categorized into geometric and non-geometric TTL [7, 8]. Among the various coupling mechanisms, the first-order TTL coupling, often referred to as the ‘piston effect’, is the most significant [9]. This effect occurs when angular tilts between different optical modules result in apparent path length changes due to the non-perfect overlap of laser beams. The primary contributors to this coupling include the alignment of the telescope, optical bench, and test masses in the interferometric system. These misalignments can introduce length noise that dominates over the desired gravitational wave signals.

To mitigate this issue, the LISA team has proposed the use of a dedicated beam alignment mechanism (BAM) to actively adjust the optical alignment and reduce TTL coupling [10, 11]. The BAM was designed to suppress the TTL coupling coefficient of the scientific interferometer from 8.5 mm/rad to 2.3 mm/rad [2]. In TianQin mission, the interstellar displacement sensitivity requirement is higher, the TTL suppression requirement is higher, and the technical challenge is greater [12].

Currently, the BAM is in its conceptual design phase, and comprehensive theoretical analyses or experimental validations of its performance are still lacking. The most significant challenge in implementing BAM lies in achieving precise two-dimensional lateral position adjustment of an Optical axis while maintaining its constant optical path length. This necessitates the ability to make millimeter-scale adjustments with micron-level precision, a requirement that pushes the limits of current optical and mechanical design. Furthermore, the mechanism must operate in the harsh environment of space, where thermal fluctuations and mechanical stresses add further complexity to maintaining alignment.

In this study, we investigate the application of a BAM as a potential solution for mitigating first-order TTL noise. The BAM employs parallel glass windows to dynamically adjust and correct the beam path. By fine-tuning these components, we aim to minimize transverse displacement and thereby reduce first-order TTL coupling.

The paper is organized as follows. Section 2 provides a theoretical analysis of effects associated with BAM. Numerical simulations were also performed to calculate the corresponding outcomes. Section 3 details experiments involving CCD testing to investigate the compensation range of BAM. Section 4 describes the design of a dual-beam interferometry apparatus to validate BAM’s suppression effect on first-order TTL coupling. Finally, Section 5 contains the conclusions and discussion.

## 2. Theory model

In the space gravitational wave interferometer system, the BAM employs a dual window design to maintain a constant optical path length. A laser beam passes obliquely through the surface parallel windows, and by controlling the rotation angle of the two windows, the lateral position of the optical axis is adjusted. Additionally, to enable arbitrary adjustments of the optical axis position within a two-dimensional plane, each window is designed to operate independently.

### 2.1. Ideal model

The schematic of the BAM is shown in Figure 1. The target laser beam passes through two surface parallel glass windows at an oblique angle, resulting in a lateral displacement of the optical axis. In this simplified model, the glass surfaces are parallel, and the rotation axis aligns with the incident optical axis. Therefore, the exiting optical axis is parallel and symmetric to the incident optical axis. For the first plate, the incident

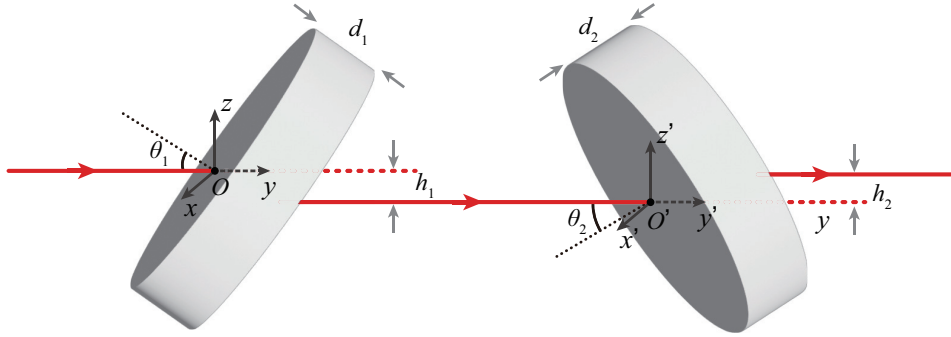


**Figure 1.** Optical schematic of the BAM, consisting of two independently inclined windows that adjust the laser beam's lateral position.

beam has thickness  $d_1$  and refractive index  $n_1$  at an incidence angle of  $\theta_1$ . The lateral displacement of the optical axis,  $\vec{h}_1$ , is given by:

$$h_1 = d_1 \sin \theta_1 \left( 1 - \frac{\cos \theta_1}{\sqrt{n_1^2 - \sin^2 \theta_1}} \right). \quad (1)$$

Figure 2 illustrates the relationship between lateral displacement and incidence angle  $\theta$ . In the range of  $0^\circ$  to  $10^\circ$ , lateral displacement increases approximately linearly. By adjusting the thickness of the glass window and the angle of incidence, the BAM's compensation range can be finely controlled. This allows for precise lateral adjustments of the optical axis, essential for space-based gravitational wave detection missions.

In the  $x$ - $O$ - $z$  plane, the compensation direction is defined as the angle  $\varphi'_1$  between the refracted beam and the  $-z$  axis. The angle between the normal vector of the window surface and the  $z$  axis is denoted as  $\varphi$ . As the glass window rotates around the optical

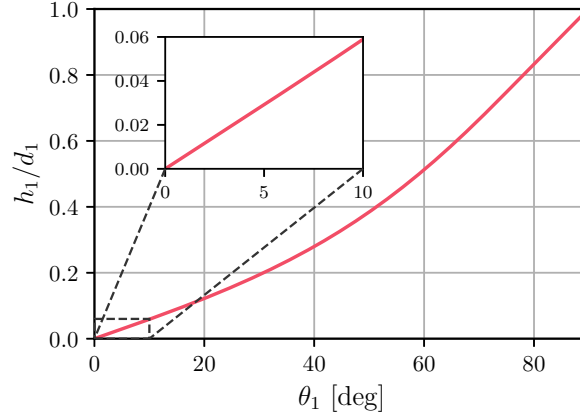


**Figure 2.** Relationship between the lateral displacement  $h$  and the incidence angle  $\theta$ .

axis, the lateral displacement amplitude remains constant, while its direction rotates by the same angle, satisfying:

$$\varphi'_1 = \varphi_1. \quad (2)$$

As a result, the position of the exiting optical axis traces a circular trajectory of radius  $h$  around the incident optical axis. In space-based gravitational wave detection, the optical-axis compensation must be adjusted in two lateral degrees of freedom. Thus, we need a second glass window.

In a new coordinate system  $x'-O-z'$ , similar to the first plate, the lateral displacement of the optical axis and compensate angle are given by:

$$h_2 = d_2 \sin \theta_2 \left( 1 - \frac{\cos \theta_2}{\sqrt{n_2^2 - \sin^2 \theta_2}} \right), \quad (3)$$

$$\varphi'_2 = \varphi_2. \quad (4)$$

The total lateral displacement of the optical axis  $h$  is the sum of the lateral displacements produced by the dual windows, given by:

$$\vec{h} = \vec{h}_1 + \vec{h}_2. \quad (5)$$

By adjusting the parameters  $d_1$ ,  $d_2$ ,  $n_1$ ,  $n_2$ ,  $\theta_1$  and  $\theta_2$  to ensure  $h_1 = h_2$ , the position of the exiting optical axis of the BAM resides within a circle centered at point  $O$  with a radius of  $2h_1$ , as shown in Figure 3. Assuming ideal conditions with  $d_1 = d_2 = 3$  mm,  $n_1 = n_2 = 1.45$ , and  $\theta_1 = \theta_2 = 8.5^\circ$ , the resulting compensation radius  $h_0$  is about 140  $\mu\text{m}$ .

## 2.2. Error analysis

Two key factors affect the practical adjustment of the BAM's optical axis compensation. First, if the rotation axis is not perfectly aligned with the incident optical axis, the compensation of the outgoing beam will vary. Second, any deviation from parallelism between the two surfaces of the glass window leads to a misalignment between the

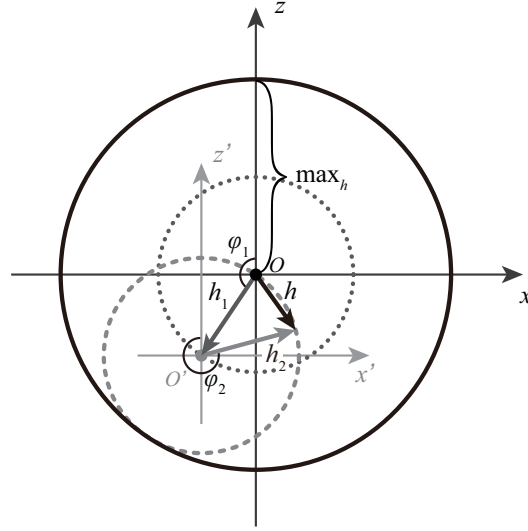


**Figure 3.** Compensation coverage of the BAM.  $\vec{h}_1$  represents the compensation position of the first window, and  $O'$  is the endpoint of  $\vec{h}_1$ . This vector can rotate as an angle  $\varphi_1$  within the  $x$ - $O$ - $z$  plane around point  $O$  as the window rotates, forming a compensation range that is a circle with center  $O$  and radius  $h_1$ . Similarly,  $\vec{h}_2$  is the compensation position of the second window, forming a circular compensation range with center  $O'$  and radius  $h_2$ . When the two windows are combined, the overall compensation position is denoted as  $\vec{h}$ . Since both windows can rotate independently, the final compensation range forms an annulus centered at  $O$ , with radii ranging from  $|h_1 - h_2|$  to  $|h_1 + h_2|$ .

incident and exiting beams. In this analysis, we assume that the glass window surfaces are sufficiently flat to minimize additional distortion.

*2.2.1. Axis misalignment* In cases where the rotation axis is misaligned by an angle  $\delta\theta$  relative to the incident optical axis, as shown in Figure 4, the compensation behavior of the beam is altered. A coordinate system is defined with the point of incidence  $O$  as the origin, and the incident beam propagating along the  $y$  axis. The unit vectors  $\vec{x}$ ,  $\vec{y}$  and  $\vec{z}$  represent the axes of this coordinate system.

The rotation axis can be defined by its direction vector  $\vec{n}_{\text{axis}}$  and a point  $A$  on the rotation axis, as follows:

$$\begin{cases} A = (x_A, y_A, z_A) \\ \vec{n}_{\text{axis}} = (n_x, n_y, n_z)^T, \end{cases} \quad (6)$$

which satisfies the conditions:

$$\begin{cases} |\vec{n}_{\text{axis}}| = 1 \\ \frac{\vec{n}_{\text{axis}} \cdot \vec{y}}{|\vec{n}_{\text{axis}}||\vec{y}|} = \cos \delta\theta. \end{cases} \quad (7)$$

Follow the Rodrigues' rotation formula, the rotation matrix  $\mathbf{R}(\vec{n}_{\text{axis}}, \varphi)$  for an angle  $\varphi$  around the rotation axis is:

$$\mathbf{R} = \mathbf{I} + \sin \varphi \mathbf{K} + (1 - \cos \varphi) \mathbf{K}^2, \quad (8)$$

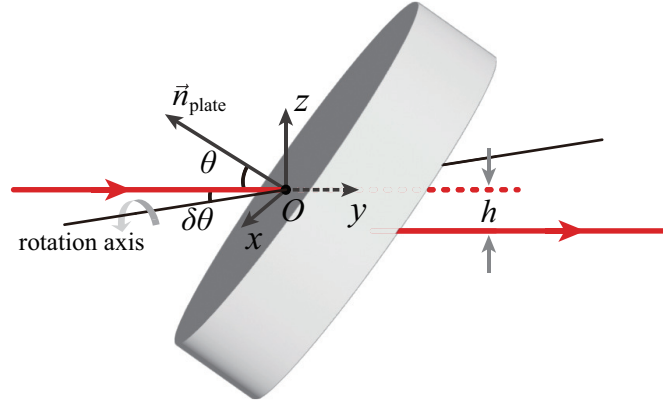


**Figure 4.** Axis Misalignment: The window's rotation axis is misaligned by an angle  $\delta\theta$  relative to the beam axis.

where  $\mathbf{I}$  is the identity matrix and  $\mathbf{K}$  is the cross-product matrix of  $\vec{n}_{\text{axis}}$ :

$$\mathbf{K} = \begin{pmatrix} 0 & -n_z & n_y \\ n_z & 0 & -n_x \\ -n_y & n_x & 0 \end{pmatrix}. \quad (9)$$

Initially, the normal vector of the glass window surface lies in the  $y$ - $O$ - $z$  plane as

$$\vec{n}_{\text{plate}} = (0, \cos \theta_0, \sin \theta_0)^T. \quad (10)$$

After rotation, the new normal vector is given by:

$$\vec{n}'_{\text{plate}} = \begin{pmatrix} x \\ y \\ z \end{pmatrix} + \mathbf{R}(\vec{n}_{\text{axis}}, \varphi) \cdot \left( \vec{n}_{\text{plate}} - \begin{pmatrix} x \\ y \\ z \end{pmatrix} \right) = (n'_x, n'_y, n'_z)^T, \quad (11)$$

Replacing  $\vec{n}_{\text{plate}}$  with  $\vec{n}'_{\text{plate}}$ , the incident angle  $\theta$  can be expressed as a function of the rotation angle  $\varphi$ :

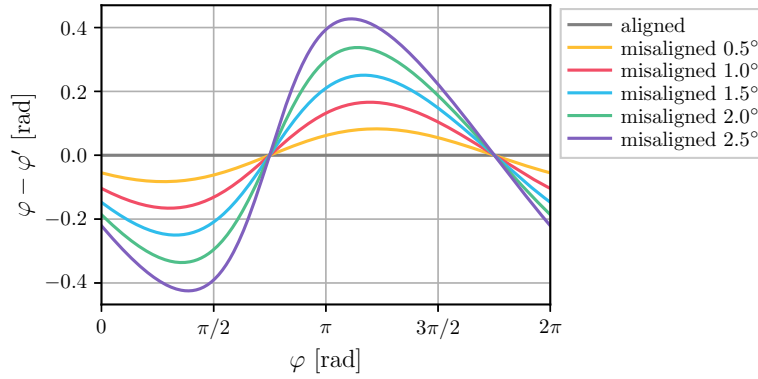
$$\theta(\varphi) = \arccos \frac{\vec{n}'_{\text{plate}} \cdot \vec{y}}{|\vec{n}'_{\text{plate}}| |\vec{y}|}. \quad (12)$$

Since the surfaces of the glass window remain parallel,  $\theta(\varphi)$  affects both the magnitude and direction of the optical axis compensation as follows:

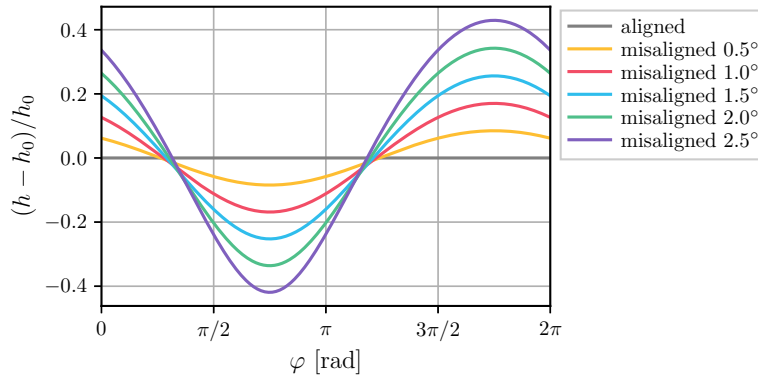
$$\begin{cases} h'(\varphi) = d \sin \theta \left( 1 - \frac{\cos \theta}{\sqrt{n^2 - \sin^2 \theta}} \right) \\ \varphi' = \arctan \frac{n'_x}{n'_z} \end{cases} \quad (13)$$

Figure 5, 6, and 7 show the simulation results of the compensation angle and radius fluctuate as the rotation angle  $\varphi$  increases, with the magnitude of these fluctuations growing as the misalignment angle increases. For small misalignment angles, the compensation range remains nearly circular. However, as the misalignment angles increase, the center of the circular compensation range shifts along the  $z$ -axis and  $x$ -axis, respectively, as shown in Figure 7. This analysis demonstrates that even slight

axis misalignment can lead to significant variations in the compensation performance of BAM.



**Figure 5.** Simulation of the compensation angle with axis misalignment.  $\varphi$  is the rotation angle of the window, and  $\varphi'$  is the compensation angle.



**Figure 6.** Simulation of the compensation radius with axis misalignment.  $\varphi$  is the rotation angle of the window, and  $h$  is the compensation radius, with  $h_0$  as the ideal compensation radius.

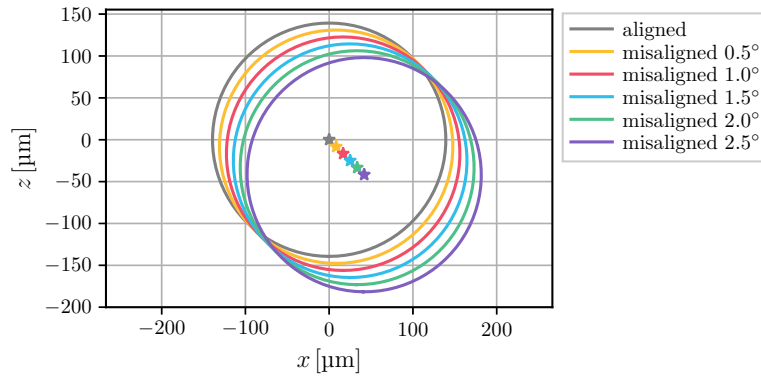


**Figure 7.** Simulation of the compensation range with axis misalignment. Asterisks indicate the fitted centers of the corresponding compensation ranges.

2.2.2. *Surface parallelism error* The second factor affecting beam alignment is the non-parallelism of the glass window surfaces, as illustrated in figure 8. In this scenario, the window thickness is defined as the distance between the two surfaces. The parallelism error, denoted as  $\alpha$ , represents the angle between the surfaces, which introduces a misalignment between the incident and exiting beams, denoted by  $\beta$ . The normal vector of the front surface is defined as:

$$\vec{n}_{\text{plateA}} = (0, \cos \theta, \sin \theta)^T. \quad (14)$$

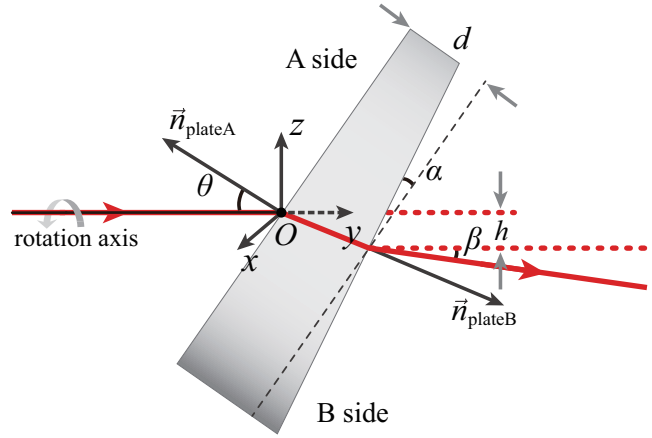


**Figure 8.** The surface parallelism error caused by the window's wedge angle  $\alpha$ , leading to a beam-axis tilt  $\beta$ .

The normal vector of the second surface is given by:

$$\begin{aligned} \vec{n}_{\text{plateB}} &= \mathbf{R}(\vec{n}_{\text{plateA}}, \phi) \cdot (0, \cos(\theta - \alpha), \sin(\theta - \alpha))^T \\ &= \begin{pmatrix} -\sin \phi \sin \theta \cos \theta_1 + \sin \phi \cos \theta \sin \theta_1 \\ (1 - (1 - \cos \phi) \sin^2 \theta) \cos \theta_1 + (1 - \cos \phi) \sin \theta \cos \theta \sin \theta_1 \\ (1 - \cos \phi) \sin \theta \cos \theta \cos \theta_1 + (1 - (1 - \cos \phi) \cos^2 \theta) \sin \theta_1 \end{pmatrix}, \end{aligned} \quad (15)$$

where  $\theta_1 = \theta - \alpha$  and  $\phi$  is the angle between the projected vector of  $\vec{n}_{\text{plateA}}$  in the  $x$ - $O$ - $z$  plane and the  $z$  axis.

According to the equation (11), the two surfaces normal vector  $\vec{n}'_{\text{plate0}}$  after rotation around the rotation axis with glass window can be expressed as:

$$\vec{n}'_{\text{plateA}} = \mathbf{R}(\vec{y}, \varphi) \cdot \vec{n}_{\text{plateA}} = \begin{pmatrix} \sin \varphi \sin \theta \\ \cos \theta \\ \cos \varphi \sin \theta \end{pmatrix}, \quad (17)$$

$$\vec{n}'_{\text{plateB}} = \mathbf{R}(\vec{y}, \varphi) \cdot \vec{n}_{\text{plateB}} \quad (18)$$

The direction of the exiting beam after refraction can be calculated using Snell's law, leading to the compensation value and angle:

$$\vec{b}_{\text{out}} = \frac{\vec{b}_{\text{in}}}{n} + \left( \frac{\cos \theta}{n} - \sqrt{1 - \frac{1 - \cos^2 \theta}{n^2}} \right) \vec{n}_{\text{plate}} = \mathbf{M}(\vec{n}_{\text{plate}}) \cdot \vec{b}_{\text{in}}, \quad (19)$$



here,  $\mathbf{M}(\vec{n}_{\text{plate}})$  represents the directional transformation of the beam after refraction through the plate. After the beam undergoes refraction twice—once at the front and once at the rear surface of the glass window—the direction vector of the exiting light can be determined. The compensation value and angle are calculated similarly to the equation (1) and (2) as:

$$\begin{cases} h' = d \sin \theta \left( 1 - \frac{\cos \theta}{\sqrt{n^2 - \sin^2 \theta}} \right) \\ \varphi' = \varphi \\ \vec{b}_{\text{exit}} = \mathbf{M}(\vec{n}'_{\text{plateB}}) \cdot \mathbf{M}(\vec{n}'_{\text{plateA}}) \cdot \vec{y} \end{cases} \quad (20)$$

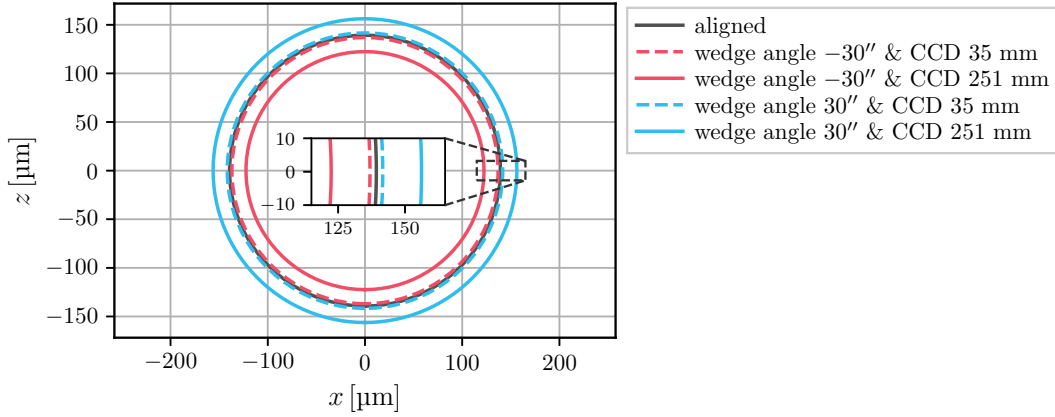


**Figure 9.** Simulation of the compensation range with surface parallelism error. solid lines and dashed lines represent opposite directions of the window wedge angle.

The surface parallelism error, as illustrated in figure 9, arises from the wedge angle of the window. When the window is fixed, the wedge angle is characterized by the normal vector of surface B, represented as  $\vec{n}_{\text{plateB}}$ . The projection of  $\vec{n}_{\text{plateB}}$  onto the  $x$ - $O$ - $z$  plane can vary in any direction. Therefore, the surface parallelism error depends on both the wedge angle's magnitude and the orientation of  $\vec{n}_{\text{plateB}}$ . The wedge angle determines the amount of tilt introduced to the optical axis, while the orientation of  $\vec{n}_{\text{plateB}}$  defines the direction of the tilt. In the simulation, the wedge angle is set to  $30''$ , and  $\vec{n}_{\text{plateB}}$  is positioned within the  $x$ - $O$ - $z$  plane.

The simulation results indicate that the surface parallelism error induces a consistent tilt in the beam axis, with the direction of this tilt governed by the orientation of  $\vec{n}_{\text{plateB}}$ . In this context, larger wedge angles result in greater beam axis deviation.

*2.2.3. Axis misalignment & surface parallelism error* In scenarios where axis misalignment and surface parallelism error occur simultaneously, these factors interact to affect the effectiveness of the compensation mechanism. The misalignment of the rotation axis by an angle  $\delta\theta$ , coupled with the deviation of the glass window surfaces by an angle  $\alpha$ , results in complex distortions of the incident and exiting beams.

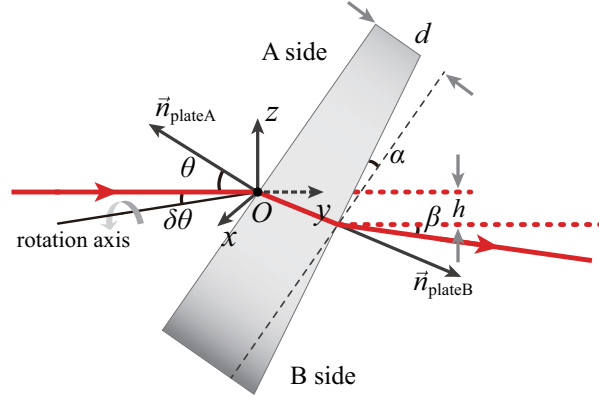


**Figure 10.** The optical schematic of both axis misalignment and surface parallelism error.

By combining the insights from Sections 2.2.1 and 2.2.2, we can derive the normal vectors for the front and rear surfaces as the glass window rotates around the axis:

$$\vec{n}'_{\text{plateA}} = \mathbf{R}(\vec{n}_{\text{axis}}, \varphi) \cdot \vec{n}_{\text{plateA}}, \quad (21)$$

$$\vec{n}'_{\text{plateB}} = \mathbf{R}(\vec{n}_{\text{axis}}, \varphi) \cdot \mathbf{R}(\vec{n}_{\text{plateA}}, \phi) \cdot \vec{n}_{\text{plateB}}. \quad (22)$$

The compensation value and angle can be expressed using equations (12) and (13):

$$\begin{cases} h'(\phi) = d \sin \theta \left( 1 - \frac{\cos \theta}{\sqrt{n^2 - \sin^2 \theta}} \right) \\ \varphi' = \arctan \frac{n'_x}{n'_z} \\ \vec{b}_{\text{exit}} = \mathbf{M}(\vec{n}'_{\text{plateB}}) \cdot \mathbf{M}(\vec{n}'_{\text{plateA}}) \cdot \vec{y} \end{cases} \quad (23)$$

Consequently, the compensation values and angles must be adjusted to account for these combined errors. Comprehensive modeling and calibration may be necessary to mitigate these effects in practical applications, ensuring that the optical system maintains the precision and accuracy required for demanding tasks such as gravitational wave detection.

### 3. Beam alignment tests

#### 3.1. Optical setup

The optical setup for beam alignment tests has been meticulously designed to evaluate the performance and precision of the BAM. Schematic diagram of the BAM experiment is shown in figure 11. Central to this experiment are two identical K9 glass windows measuring  $10 \text{ mm} \times 10 \text{ mm} \times 3 \text{ mm}$ . These windows are mounted at an angle on high-precision motorized rotation stages, which provide angular control with a resolution of about  $0.05^\circ$ . This level of precision enables fine adjustments to the beam path, essential for achieving accurate alignment.

Initially, the glass windows are set at an approximate angle of  $8.5^\circ$  relative to the incident beam, facilitating effective control of beam displacement during rotation. The two BAM components are arranged sequentially in the optical path following a laser collimator, with a CCD camera beam profiler positioned downstream of the second BAM component. This configuration allows for high-precision monitoring of the beam position, thereby enabling accurate measurement of beam displacement resulting from the combined effects of the BAM.

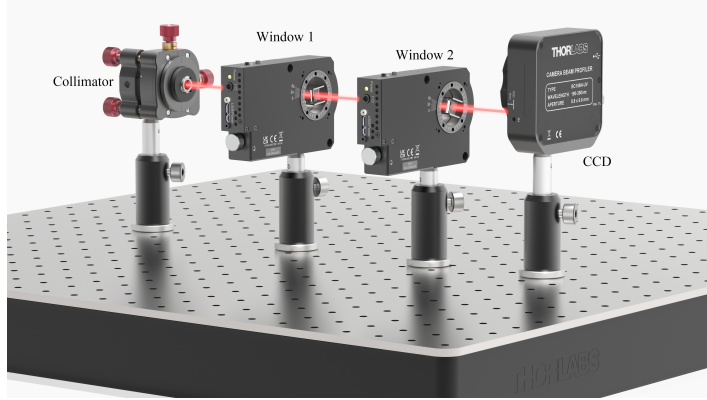


**Figure 11.** Schematic diagram of the BAM for experimental validation. The Gauss beam, originating from the collimator on the left, sequentially traverses through dual windows positioned on a rotation stage, ultimately being detected by the CCD. The rotational axis is adjusted using a tip, tilt, and rotation stage (not shown) beneath the rotation stage to align as closely as possible with the beam axis. When the two rotational mountings move independently, the beam experiences lateral displacement within a plane constrained by a circular range.

System control and data acquisition are managed by two specialized programs, which interface with the rotation mounts and CCD camera respectively. The software employs image processing algorithms to determine the centroid position of the beam spot on the CCD sensor, allowing for precise tracking of beam displacement relative to the pane rotation angles. The centroid position  $(x_c, z_c)$  is calculated using the weighted average method:

$$x_c = \frac{\sum_i \sum_j x_{ij} I_{ij}}{\sum_i \sum_j I_{ij}}, \quad z_c = \frac{\sum_i \sum_j z_{ij} I_{ij}}{\sum_i \sum_j I_{ij}} \quad (24)$$

where  $x_{ij}$  and  $z_{ij}$  are the coordinates of pixel  $(i, j)$ , and  $I_{ij}$  is the intensity of that pixel. This method provides a robust and accurate determination of the beam position, accounting for variations in beam shape and intensity distribution.

### 3.2. Test results

To comprehensively assess the performance of the Beam Alignment Mechanism (BAM), we structured our experiments into three distinct parts: (1) evaluating the effects of axis misalignment using a single window, (2) analyzing the impacts of surface parallelism

using a single window, and (3) investigating the combined effects of axis alignment with dual windows. Each experiment tracks the beam center across a full rotation of the windows, referred to as the compensation range.

In the initial experiments, we isolated the effects of individual components by removing one of the windows from the setup. This adjustment allowed for a clearer understanding of how each factor contributes to beam alignment.

The first experiment focused on the axis misalignment effect. We minimized the distance between the CCD camera and the window to 35 mm to enhance measurement sensitivity. The results of this setup are shown in figure 12, where the gray line represents the compensation range with axis alignment, while the blue and red lines indicate results with pitch and yaw misalignments of  $0.55^\circ$  and  $1.10^\circ$ , respectively. The fitted centers of the corresponding compensation ranges are denoted by asterisks.

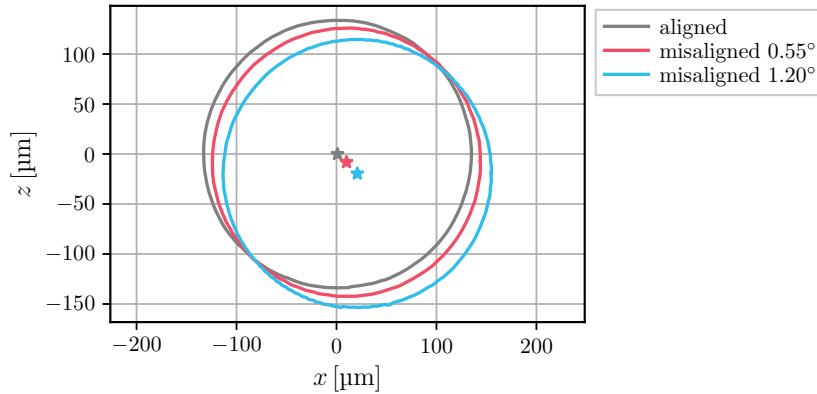


**Figure 12.** Compensation range with axis misalignment for a single plate. The gray line represents results with axis alignment, while the blue and red lines show results with both pitch and yaw angles of  $0.55^\circ$  and  $1.10^\circ$ , respectively. Asterisks indicate the fitted centers of the corresponding compensation ranges.

Next, we examined the influence of surface parallelism error on beam alignment. As depicted in figure 13, the rotation axis was pre-aligned to the optical axis, allowing us to analyze the tilt induced in the exiting beam due to misalignment between the front and rear surfaces of the window. We compared the compensation ranges at CCD distances of 35 mm and 251 mm, observing how this configuration affected beam behavior.

In the third experiment, we explored the combined effects of axis alignment using two rotating windows. The setup, depicted in figure 14, was designed to create a spiral-like displacement pattern. As the two windows rotated at different angular velocities, the compensation range accumulated, forming an area constrained within a circular path. This design allowed us to visualize the cumulative impact of both windows on beam alignment.

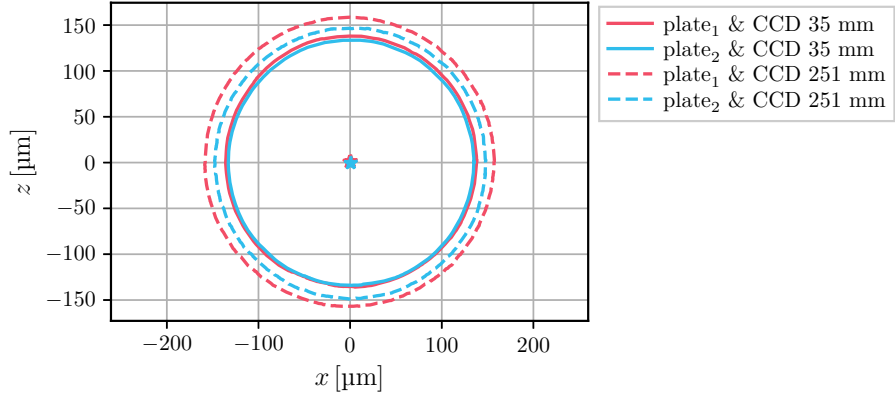


**Figure 13.** Compensation range with surface parallelism error for a single plate. Red and blue lines represent two different windows, with solid and dashed lines indicating distances of 35 mm and 251 mm between the CCD camera and the window, respectively.

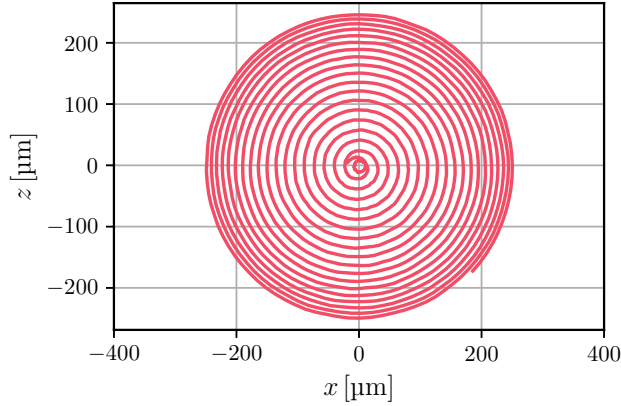


**Figure 14.** Compensation range with axis alignment for dual windows. The setup rotates two windows at different angular velocities over a period, creating a spiral-like pattern. Over time, the compensation range accumulates, forming a circular area with a radius of 250  $\mu\text{m}$ .

## 4. TTL tests

In previous sections, we have established the compensation range of the BAM structure for both single and dual window configurations, particularly under the influence of axis and surface parallelism errors. This section delves into the application of BAM for inducing lateral displacement in interferometry to suppress first-order tilt-to-length (TTL) coupling.

### 4.1. Optical setup

The experimental setup is based on a compact heterodyne interferometer, designed for high-precision measurement and simplified system architecture [13]. The interferometer is assembled using UV bonding technology, which enhances mechanical stability and ensures long-term alignment precision [14, 15]. The optical schematic of TTL coupling

suppressing by BAM is illustrated in figure 15. The system utilizes two heterodyne beams, differing by 10 kHz in frequency. These beams are introduced through collimators and directed through distinct optical paths.

One beam is reflected off a stable reference mirror before being combined with the second beam at beam splitter  $BS_1$ , producing a reference signal that is detected by photodetector  $PD_r$ . The second beam traverses the BAM, undergoes reflection from a target mirror, and retraces its path back through the BAM. Finally, the beams recombine at beam splitter  $BS_2$ , with the resulting interference signal captured by photodetector  $PD_m$ .

The primary factor influencing first-order TTL coupling is the lateral displacement between the beam's reflection point on the target mirror and the mirror's rotation axis. A 6-axis Hexapod (PI-H811) is employed to control and fine-tune the target mirror's rotation axis. The BAM allows precise adjustments to the beam position on the target mirror, effectively compensating for first-order TTL coupling errors and enhancing the overall measurement accuracy.

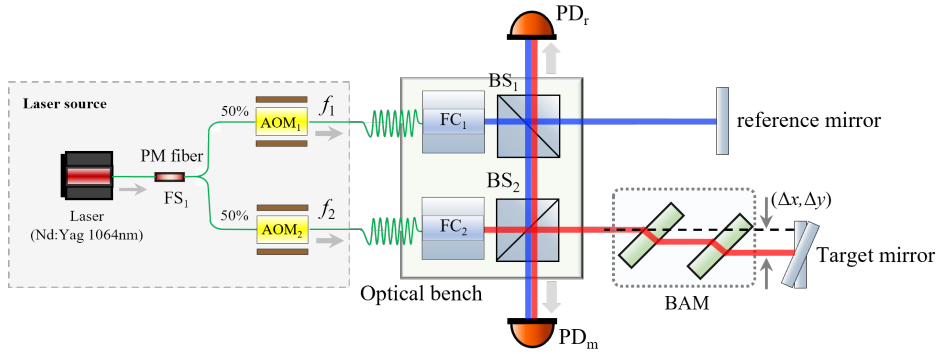


**Figure 15.** The optical schematic of the TTL coupling suppressing by BAM.

#### 4.2. Test results

The results of the TTL tests are illustrated in Figure 16, which clearly shows the effectiveness of the BAM in reducing first-order TTL coupling errors. Initially, the TTL coupling coefficient was measured at approximately  $300 \mu\text{m}/\text{rad}$ . As the BAM was employed to adjust and align the beam axis, a gradual decrease in this coupling error was observed. By meticulously fine-tuning the lateral displacement of the beam axis, the coupling coefficient was ultimately reduced to an impressive  $5 \mu\text{m}/\text{rad}$ . Further first-order TTL coupling suppression is limited by the optical axis tuning accuracy of the BAM and the displacement measurement noise floor of the interferometer bench.

This significant reduction underscores the BAM's potential to enhance measurement precision in interferometric systems, particularly in the context of gravitational wave detection. The experimental data aligns well with theoretical predictions, demonstrating that the BAM can effectively manage the adverse effects of misalignment and

surface errors. Such capabilities are crucial for improving the performance of gravitational wave detectors, where minimizing noise is essential for accurate measurements.

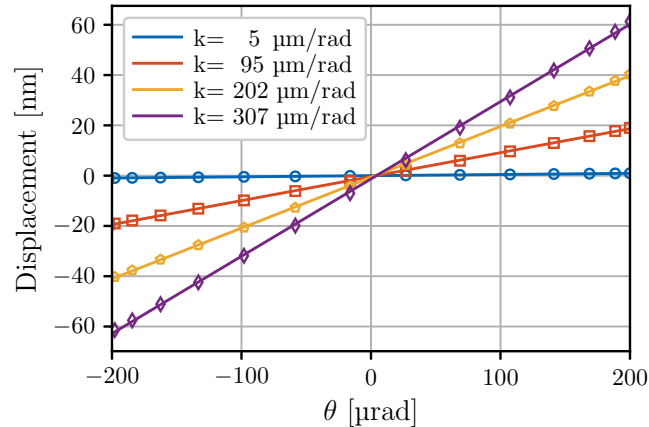


**Figure 16.** TTL coupling test results, showing the TTL coupling curve with angle. The maker represents the experimental data, and the line represents the fitting curve.

## 5. Discussion and conclusion

This study explored the Beam Alignment Mechanism’s (BAM) ability to mitigate tilt-to-length (TTL) coupling noise in gravitational wave detectors. The experimental results affirm that BAM significantly compensates for lateral displacement errors, effectively aligning the optical axis and reducing TTL noise. However, challenges remain due to misalignments that can introduce additional tilts, potentially affecting suppression efficiency. While current configurations show promise, further optimization is necessary.

In conclusion, BAM represents a substantial advancement in addressing TTL noise, enhancing the precision of interferometric measurements. Ongoing research into alignment techniques and adaptive control algorithms will be vital in refining BAM’s effectiveness. By overcoming existing limitations, BAM can play a pivotal role in the next generation of gravitational wave detectors, supporting efforts to observe the universe’s most elusive phenomena.

## Reference

- [1] LIGO Scientific Collaboration and KAGRA Collaboration V C, Abbott R, Abbott T, Acernese F, Ackley K *et al.* 2023 *Physical Review X* **13** 041039 publisher: American Physical Society URL <https://doi.org/10.1103/PhysRevX.13.041039>
- [2] Colpi M, Danzmann K, Hewitson M, Holley-Bockelmann K, Jetzer P *et al.* 2023 LISA Definition Study Report arXiv:2402.07571 [astro-ph, physics:gr-qc] URL <https://doi.org/10.48550/arXiv.2402.07571>
- [3] Luo J, Chen L S, Duan H Z, Gong Y G, Hu S *et al.* 2016 *Classical and Quantum Gravity* **33** 035010 ISSN 0264-9381 publisher: IOP Publishing URL <https://doi.org/10.1088/0264-9381/33/3/035010>

- [4] Mei J, Bai Y Z, Bao J, Barausse E, Cai L *et al.* 2021 *Progress of Theoretical and Experimental Physics* **2021** 05A107 ISSN 2050-3911 URL <https://doi.org/10.1093/ptep/ptaa114>
- [5] Hu W R and Wu Y L 2017 *National Science Review* **4** 685–686 ISSN 2095-5138 URL <https://doi.org/10.1093/nsr/nwx116>
- [6] Luo Z, Wang Y, Wu Y, Hu W and Jin G 2021 *Progress of Theoretical and Experimental Physics* **2021** 05A108 ISSN 2050-3911 URL <https://doi.org/10.1093/ptep/ptaa083>
- [7] Hartig M S, Schuster S and Wanner G 2022 *Journal of Optics* **24** 065601 ISSN 2040-8978, 2040-8986 URL <https://doi.org/10.1088/2040-8986/ac675e>
- [8] Hartig M S, Schuster S, Heinzel G and Wanner G 2023 *Journal of Optics* **25** 055601 ISSN 2040-8978, 2040-8986 URL <https://doi.org/10.1088/2040-8986/acc3ac>
- [9] Paczkowski S, Giusteri R, Hewitson M, Karnesis N, Fitzsimons E D *et al.* 2022 *Physical Review D* **106** 042005 ISSN 2470-0010, 2470-0029 URL <https://doi.org/10.1103/PhysRevD.106.042005>
- [10] Brzozowski W *et al.* 2022 The LISA optical bench: an overview and engineering challenges *Space Telescopes and Instrumentation 2022: Optical, Infrared, and Millimeter Wave* vol 12180 ed Coyle L E, Matsuura S and Perrin M D International Society for Optics and Photonics (SPIE) p 121800O URL <https://doi.org/10.1117/12.2627465>
- [11] Colpi M *et al.* 2024 Lisa definition study report (*Preprint* 2402.07571) URL <https://arxiv.org/abs/2402.07571>
- [12] Gong Y, Luo J and Wang B 2021 *Nature Astronomy* **5** 881–889 ISSN 2397-3366 publisher: Nature Publishing Group URL <https://doi.org/10.1038/s41550-021-01480-3>
- [13] Yan H, Mao Q, Xie S, Liu S, Luo J *et al.* 2020 *Optics Letters* **45** 2792–2795 ISSN 1539-4794 publisher: Optica Publishing Group URL <https://doi.org/10.1364/OL.392856>
- [14] Lin X, Yan H, Miao H X, Qiu P, Liang Y R *et al.* 2024 *Optics Express* **32** 37167–37181 ISSN 1094-4087 publisher: Optica Publishing Group URL <https://doi.org/10.1364/OE.539457>
- [15] Lin X, Yan H, Ma Y and Zhou Z 2023 *Review of Scientific Instruments* **94** 074501 ISSN 0034-6748 URL <https://doi.org/10.1063/5.0155637>